addenda and errata

Weblinks for the Daresbury Laue software source code and information. Addendum

Quan Hao,[a]* Marjorie M. Harding,[b]* John R. Helliwell[c]* and D. Marian Szebenyi[d]*

[a]School of Biomedical Sciences, University of Hong Kong, Hong Kong, [b]Centre for Translational and Chemical Biology, University of Edinburgh, Michael Swann Building, Mayfield Road, Edinburgh EH9 3JR, United Kingdom, [c]Department of Chemistry, University of Manchester, Manchester M13 9PL, United Kingdom, and [d]MacCHESS, Cornell University, Ithaca, New York, USA.*Correspondence e-mail: qhao@hku.hk, marjorieharding80@gmail.com, john.helliwell@manchester.ac.uk, dms35@cornell.edu

The weblinks for the Daresbury Laue software source code and information have become hidden from a simple google search. This Addendum makes clear where the software source code and information can now be found.

The software source code (identical versions) may be downloaded from any one of the following three weblinks:

https://www.chess.cornell.edu/sites/default/files/inline-files/Daresbury_laue.tar.gz

https://zenodo.org/record/4381992#.X-B7Z1DgrtQ

http://web.hku.hk/~qhao/Daresbury_laue_Dec2020.tar.gz

The weblink for the full information about the suite is now https://web.archive.org/web/20001024010254/http://www.dl.ac.uk/SRS/PX/jwc_laue/laue_top.html.

As a very brief recap, the recording and analysis of synchrotron Laue diffraction data were described in Helliwell *et al.* (1989). The finalised wavelength normalisation was described in Arzt *et al.* (1999), and the finalised integration in Campbell *et al.* (1998) includes the adaptations made for neutron Laue diffraction data collection. A summary article of the numerous benchmark applications with synchrotron radiation was Nieh *et al.* (1999), to which this addendum is attached. The conversion of the source code for use with neutron sources has been made at the Institut Laue Langevin and the Oak Ridge National Laboratory reactor and spallation sources. Access to those versions are at the discretion of those facilities. The principal funding sources involved were the UK's Science and Engineering Research Council (SERC) and the Engineering and Physical Sciences Research Council (EPSRC), Principal Investigator (PI): M. M. Harding, and Co-PI: J. R. Helliwell.

References

Arzt, S., Campbell, J. W., Harding, M. M., Hao, Q. & Helliwell, J. R. (1999). *J. Appl. Cryst.* **32**, 554–562.

Campbell, J. W., Hao, Q., Harding, M. M., Nguti, N. D. & Wilkinson, C. (1998). *J. Appl. Cryst.* **31**, 496–502.

Helliwell, J. R., Habash, J., Cruickshank, D. W. J., Harding, M. M., Greenhough, T. J., Campbell, J. W., Clifton, I. J., Elder, M., Machin, P. A., Papiz, M. Z. & Zurek, S. (1989). *J. Appl. Cryst.* **22**, 483–497.

Nieh, Y. P., Raftery, J., Weisgerber, S., Habash, J., Schotte, F., Ursby, T., Wulff, M., Hädener, A., Campbell, J. W., Hao, Q. & Helliwell, J. R. (1999). *J. Synchrotron Rad.* **6**, 995–1006.
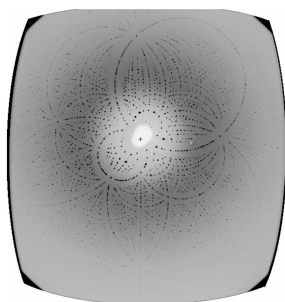
Accurate and highly complete synchrotron protein crystal Laue diffraction data using the ESRF CCD and the Daresbury Laue software

Y. P. Nieh,[a]† J. Raftery,[a] S. Weisgerber,[a] J. Habash,[a] F. Schotte,[b] T. Ursby,[b]‡ M. Wulff,[b] A. Hädener,[c] J. W. Campbell,[d] Q. Hao[e] and J. R. Helliwell[a]*

[a]*Department of Chemistry, University of Manchester, Manchester M13 9PL, UK,* [b]*European Synchrotron Radiation Facility (ESRF), BP 220, Grenoble CEDEX, France,* [c]*Departement Pharmazie, Institut für Pharmazeutische Chemie, Universität Basel, Totengässlein 3, CH-4051 Basel, Switzerland,* [d]*CLRC Daresbury Laboratory, Warrington WA4 4AD, Cheshire, UK, and* [e]*De Montfort University, Leicester LE1 9BH, UK. E-mail: john.helliwell@man.ac.uk*

Developments in electronic area detectors such as CCDs and image plates have transformed the capability of the synchrotron Laue protein crystallography technique compared with film. The rapid readout of CCDs makes practical the use of rather fine angular interval settings of the crystal between each Laue exposure and a large overall angle coverage. The use of the ESRF CCD (image intensifier type) presented here in the Laue data collection on ESRF ID09 (the 'Laue beamline') from a single crystal of the 34 kDa wild-type hydroxymethylbilane synthase (HMBS), space group $P2_12_12$ $a = 88.06$, $b = 75.73$, $c = 50.35$ Å, yielded 47 Laue exposures in 2.5° angle intervals from a *single* crystal. The data processed by the Daresbury Laue software is highly complete (∞–$2d_{min} = 77.5\%$; $2d_{min}$–$d_{min} = 91.7\%$) to 2.3 Å with high redundancy (11.2). Comparison with calculated structure factors and careful analysis of the Laue geometry shows that between ∞ and $5d_{min}$ better completeness still should be possible, which can ideally be realized from CCD detector dynamic range hardware improvements and/or software algorithms to integrate saturated spot profiles. Prospects for Laue diffraction data collection using yet faster detectors such as the 'pixel detector' to study *irreversible* catalytic structural processes in a crystal, the most challenging of all time-resolved experiments, are bright.

Keywords: detector dynamic range; CCD Laue data; Laue software; hydroxymethylbilane synthase; protein crystallography.

1. Introduction

Synchrotron radiation protein crystallography has expanded enormously as a field of activity in the last two decades including each of its sub-fields of high resolution, anomalous scattering (MAD) and dynamical (time-resolved) studies. The technical hurdles of working with small, even tiny, crystals (down to ∼10 µm size) and very large unit cells (up to ∼1000 Å) have largely been overcome. For a recent review see Chayen *et al.* (1996).

In the sub-field of time-resolved protein crystallography (Cruickshank *et al.*, 1992; Ren & Moffat, 1994; Helliwell & Rentzepis, 1997) the rapid collection of diffraction data utilizing focused monochromatic or polychromatic synchrotron radiation has opened up studies of structural processes with rate constants ranging from one per kilosecond through to one per sub-nanosecond. Within this vast range of timescales there are distinctly different details of instrumentation and methods for initiation of a chemical reaction in protein crystals. The identification of the correct moment in time for diffraction data acquisition can be either *via* a spectral signal, if one is available, *i.e.* micro-spectrophotometry, or by the repeated measurement of diffraction data over time after initiation of a structural process in the crystal. There are two distinctly different types of time-resolved study; namely, reversible and irreversible processes. The reversible processes, often initiated by light flash, offer the chance of recycling of reaction initiation, data collection, relax, reaction initiation, data collection, relax *etc*. The irreversible processes do not allow such recycling. They require different strategies for complete diffraction data set measurement, *e.g.* averaging over multiple crystals for particular time slices. Alternatively, as rapid as possible multiple crystal orientation and efficient diffraction data acquisition is needed, for which the detector and the software should be as effective as possible.

---

† Present address: Fred Hutchinson Cancer Research Centre, Seattle, USA.

‡ Present address: Department of Molecular Biophysics, University of Lund, Lund, Sweden.

In the field of detectors a massive change in capability has come with the use of CCD and IP detectors over photographic film. Enhanced DQE (detector quantum efficiency), especially for weak diffraction spots, has reduced the exposure time and/or improved data quality thus allowing, in general, many more exposures per crystal sample. On-line IPs, and of course CCDs (which are intrinsically 'on-line'), allow automatic multiple-exposure data collection. CCD readout times are smaller than those of on-line IPs, by up to orders of magnitude. To optimize the use of beam-time shifts this duty cycle is of course important (*e.g.* for MAD, see Hädener *et al.*, 1999; Peterson *et al.*, 1996; Helliwell, 1979). For the time-resolved study of irreversible processes in a crystal the advantage of rapid CCD readout is especially important; constrained, for example, by the requirement that total data collection times have not to exceed ∼100 s or less. Reversible processes, however, can be set up in multiple cycles [*e.g.* in their sub-nanosecond study of CO Mb (Srajer *et al.*, 1996)]. Fast detector readout then allows optimal diffraction data coverage. In Laue diffraction, fine angle interval setting of the crystal has now become the norm rather than the exception (*e.g.* see Yang *et al.*, 1998; Bradbrook *et al.*, 1997). The difficulty of measuring the full dynamic range of diffraction data to be collected in any one exposure on a detector is exacerbated in the Laue case. This is because a subset of the diffraction spots are now multiple and these predominantly involve low-resolution reflections (Cruickshank *et al.*, 1987) along with their higher-diffraction-order multiples. The dynamic range performance of a CCD detector in Laue diffraction data is one of the aspects explored in this paper.

In the field of Laue software the most extensively and widely used software is the Daresbury Laue software and analysis package (Helliwell, Habash *et al.*, 1989; Campbell, 1995). Before general release of this software in ∼1989 (although it was released to specific SRS users as a 'β test' version in 1986) a variety of detailed case studies were undertaken. The core issues addressed in those case studies were the data quality realizable with the wavelength normalization (*i.e.* 'λ-curve' determination) using symmetry equivalents (Campbell *et al.*, 1986) or in comparison with an existing monochromatic set. Also, deconvolution of multiples' intensities was undertaken for the first time. At that time this required 'multiple film' packs. In one case study, high-quality protein structure refinement was achieved with Laue film data; for carbonic anhydrase protein model refinement against Laue data to 2.2 Å resolution showed a single water molecule coordinated to the essential Zn atom (Lindahl *et al.*, 1992). In another study a partially occupied water molecule in myoglobin was seen (Cameron *et al.*, 1993). In other case studies, high-quality small-molecule structure refinement, including location of all H atoms (Helliwell, Gomez de Anderez *et al.*, 1989), and direct-methods structure determination (Gomez de Anderez *et al.*, 1989) were achieved. This Laue software analysis package was thereby distributed worldwide, benchmarked *via* these case studies listed above, for community use. That use has been very successful and included the first time-resolved Laue diffraction study [of the enzyme p21 by Schlichting *et al.* (1990)], a *de novo* protein crystal structure determination *via* molecular replacement (Howell *et al.*, 1992), a pH jump study of chymotrypsin (Singer *et al.*, 1993), and a time-resolved study on isocitrate dehydrogenase (Bolduc *et al.*, 1995), amongst others. For a recent review see Ren *et al.* (1999).

Laue data collection on film was exceedingly laborious. The use of IPs initially, and CCDs now, has transformed the ease of data collection and, as referred to above, increased the number of exposures measurable per sample. The dynamic range of these detection media could not readily be extended in a way akin to a multiple film arrangement, although a double image-plate arrangement (in a toast-rack style) was shown to be feasible (Helliwell, 1991). In general, however, a new method for deconvolution of multiples was needed. Measurement of a multiple reflection Laue spot at different crystal orientations, which altered the relative intensity of each component, offered an analogous method to the multiple film pack approach (Helliwell, 1992). Software was written and tested based on this idea by Campbell & Hao (1993) and subsequently by others (Ren & Moffat, 1995b). Spatial overlap of crowded (especially broad bandpass) Laue diffraction patterns was less of a problem than energy multiples, except perhaps for the laser light flash experiments where a shockwave passing through the protein crystal, at the speed of sound (Edwards *et al.*, 1990), caused pronounced spot streaking in certain time frames (∼µs); Ren & Moffat (1995a) especially addressed this in their Chicago software package, although this is not yet on release but has been 'β tested' at ESRF (*e.g.* Bourgeois *et al.*, 1998).

This paper describes then the utilization of the fast-readout (∼8 s) ESRF CCD detector (Moy *et al.*, 1996) in Laue diffraction data collection on ESRF ID09 (the Laue beamline). The area calibration of the device is evaluated and recommendations are made concerning the dynamic range of the detector and data-collection protocol. The Daresbury Laue software is used with the 'wavelength binning' method, along with the energy deconvolution approach of Helliwell (1992), implemented by Campbell & Hao (1993), and spatial overlap deconvolution based on the profile approach of Rossmann (1979) as implemented by Shrive *et al.* (1990) and subsequently revised by Campbell *et al.* (1998). As will be seen, accurate highly redundant and highly complete Laue diffraction data have been collected for a crystal of wild-type hydroxymethylbilane synthase (HMBS) from *E. coli* (crystal size ∼50 × 500 × 500 µm^3), for which refined coordinates and structure factors have been deposited with the PDB (access codes 2YPN and 2YPNSF). HMBS (EC 4.3.1.8) catalyses the conversion of porphobilinogen to hydroxymethylbilane, an intermediate in the biosynthesis of tetrapyrrolic pigments such as haem, chlorophyll and vitamin B12 (Battersby & Leeper, 1990).
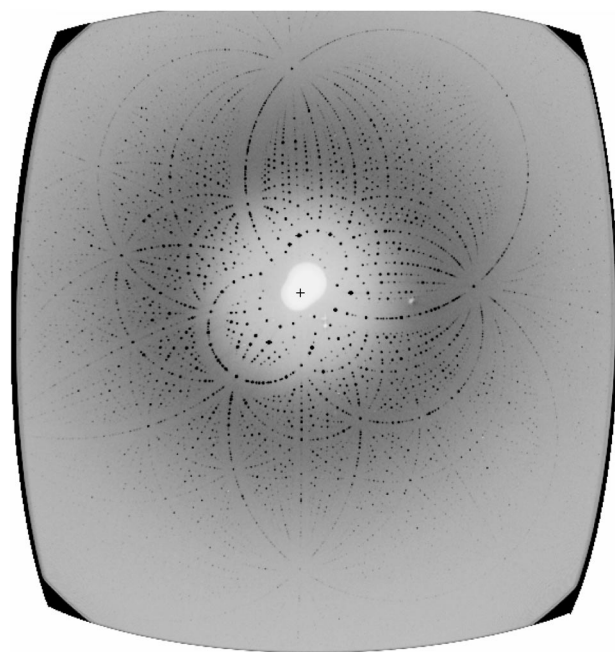
Table 1
Laue data collection.

X-ray source	ESRF ID09 (BL3)
Detector system	X-ray image intensifier/CCD†
Crystal-to-detector distance	155 mm
Wavelength range‡	0.34–1.60 Å
Number of crystals§	1
Number of images	47
Angular interval	2.5°
Total angular range	115°
Exposure time (per image)	1.5 ms

† 1152 × 1242 pixels with pixel size 0.114 × 0.114 mm². ‡ The soft limits determined by *LAUEGEN* (Campbell, 1995). § The crystal was translated after collecting ∼12 Laue images at any one position to avoid possible radiation damage. All data were collected at room temperature.

In its active reduced form the enzyme uses a dipyrromethane cofactor for catalysis. In the presence of air, the cofactor can be oxidized, rendering the enzyme catalytically inactive. Structures of both the oxidized and the reduced form of HMBS have been determined by X-ray crystallography using MIR (Louie *et al.*, 1992) and a MAD analysis of a selenomethionine-labelled variant of the protein (Hädener *et al.*, 1999), respectively. With respect to the Laue study of the reduced form of wild-type HMBS presented here, it is important to note that the molecular mass of this protein (34 kDa) is more than twice that of previously studied proteins such as phospho yellow protein, PYP (14 kDa), or myoglobin, Mb (17 kDa) (Ren & Moffat, 1995*a,b*), or restrictocin (Yang *et al.*, 1998) or lysozyme (15 kDa) (Bradbrook *et al.*, 1997). The high-quality wild-type HMBS Laue data recorded on the ESRF ID09 and this CCD in a 'static Laue' case study encouraged time-resolved structural and biophysical chemistry studies,

reported by Helliwell *et al.* (1998), of an irreversible process in the crystals of the K59Q HMBS mutant enzyme.

2. Experimental

2.1. *Crystallization of wild-type HMBS reduced form*

Sitting drops of 50 µl volume were used. Each drop contained 6–7 mg ml^{-1} of protein, 0.3 mM edta, 15 mM dithiothreitol, 10% (mass/volume) poly(ethylene glycol) 6000 and 0.01% NaN$_3$ in 0.1 M sodium acetate and was equilibrated by vapour diffusion at 293 K against a reservoir of 10–20 mg solid dithiothreitol. Further details can be found in Hädener *et al.* (1993), which reports the use of these conditions for crystallization of the active reduced form of selenomethionine-labelled HMBS.

2.2. *Laue data collection of wild-type HMBS*

A wild-type crystal of HMBS with the cofactor in the reduced form was used to collect 47 Laue images. Table 1 shows a summary of the data collection. One of the Laue patterns is shown in Fig. 1.

(a)

(b)
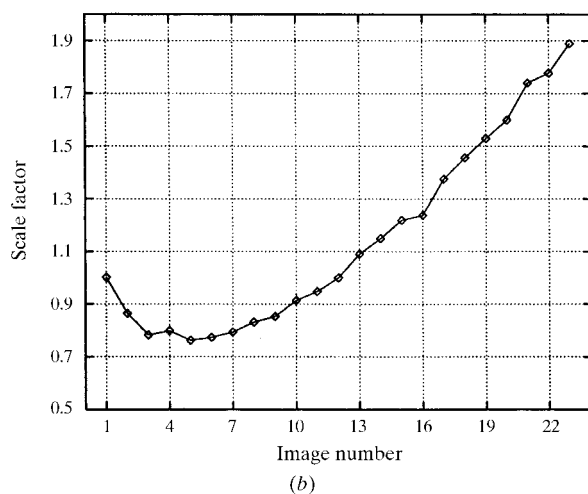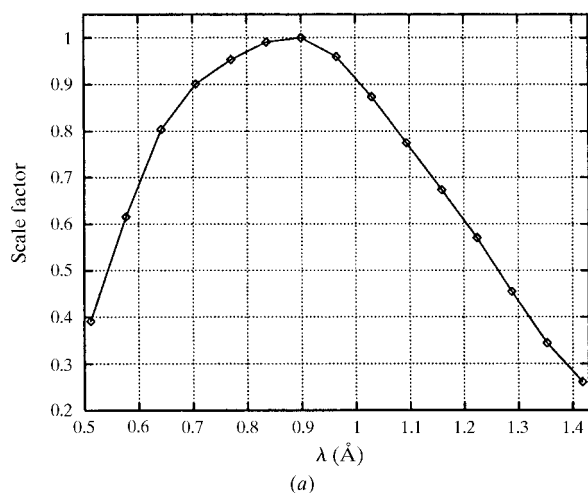
Figure 2
(*a*) Wavelength-normalization curve; (*b*) inter-image scale factors (illustrated for the case of subset I, subset II being very similar).

Figure 1
Laue diffraction pattern of a crystal of wild-type HMBS recorded on a CCD detector at ESRF ID09 (BL3).

2.3. Non-uniformity calibration of CCD images

All area X-ray detectors (except film and IPs) suffer to some extent from non-uniform intensity response to X-rays across the detecting area. Therefore, a calibration technique is needed, without which the accuracy of intensity measurement of the reflection intensities would be degraded. The X-ray image intensifier/CCD detector system currently used in ESRF ID09 (BL3) has a strong radial variation of intensity response. Moy *et al.* (1996) employed a flat-field correction method using an Sr-doped amorphous lithium glass plate, emitting isotropic fluorescence when excited by the X-ray beam. This method, developed for monochromatic data, was applied to the 47 CCD Laue images of HMBS with the calibration profile performed at the synchrotron radiation fluorescence energy of 14.2 keV (wavelength 0.87 Å).

3. Wild-type HMBS Laue data processing

The 47 Laue images of wild-type HMBS were processed using the Daresbury Laue processing suite (Helliwell, Habash *et al.*, 1989; Campbell, 1995). The procedures and results are summarized below.

LAUEGEN. The Laue images were indexed with an r.m.s. deviation of observed and calculated spot positions between 0.025 mm and 0.047 mm. The refined cell para-
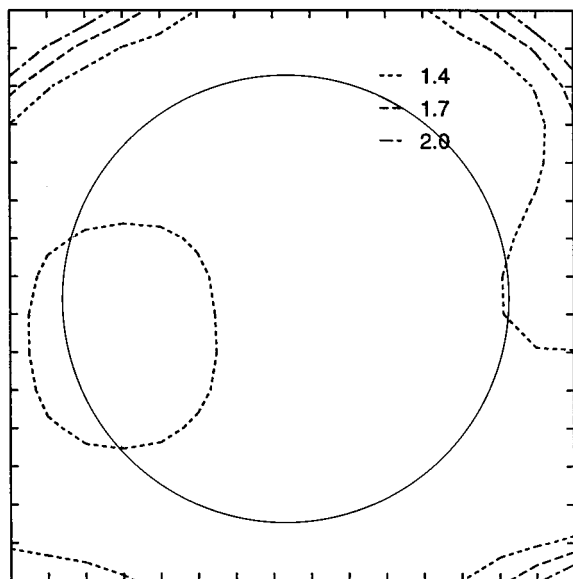

Figure 3
The residual effect (in terms of $I_{\text{reference}}/I_{\text{Laue}}$ contoured for values of 1.4, 1.7 and 2.0) after non-uniformity correction performed at one wavelength. Note that the calculation was performed by the *LAUESCALE* program (Helliwell, Habash *et al.*, 1989; Maginn *et al.*, 1993) which applies wavelength normalization and sample absorption corrections to each Laue image. Here it can be assumed that the sample absorption effect is negligible and the correction can therefore be used to estimate the non-uniformity of response of the detector. The reference data set used in the contour plot calculation was the MAD data of selenomethionine-labelled HMBS at 2.4 Å (at room temperature) (Hädener *et al.*, 1999). The circle of 55 mm radius is shown.

Table 2
Data processing statistics of wild-type HMBS Laue data.

	Full detector aperture (70 mm)	55 mm radius cut-off
LAUENORM		
Wavelength range (Å)	0.46–1.38	0.48–1.45
$N_{\text{single}}-\text{I}$†	119386	84681
$N_{\text{single}}-\text{II}$†	121171	84509
$N_{\text{multiple}}-\text{I}$†	2467	2479
$N_{\text{multiple}}-\text{II}$†	1914	1907
$R_{\text{sym}}-\text{I}$†	14.2%	10.8%
$R_{\text{sym}}-\text{II}$†	15.5%	10.6%
AGROVATA		
Completeness‡	90.7%	89.5%
Redundancy	14.5	11.2
$I/\sigma(I)$	4.6	5.9
R_{merge} §	12.2%	9.4%¶

† The data were subdivided into two sets for *LAUENORM* (for details, see text). ‡ Statistics are compared to 2.5 Å resolution. § The R_{merge} for the singles and reflection intensities from deconvoluted multiples were 10% and 6%, respectively; the superior R_{merge} for the deconvoluted multiples arising from the preponderence of strong intensities in this category [$I/\sigma(I)$ of 7.8 *versus* 5.0] also documents the effectiveness of the 'λ-curve deconvolution procedure'. The completeness for the singles only was 66% and 88% for ∞–$2d_{\text{min}}$ and ∞–d_{min}, respectively (although very similar for full *versus* 55 mm radius aperture, these numbers are for the latter case). ¶ Data were subsequently reprocessed to 2.3 Å and formed the data used in Table 3.
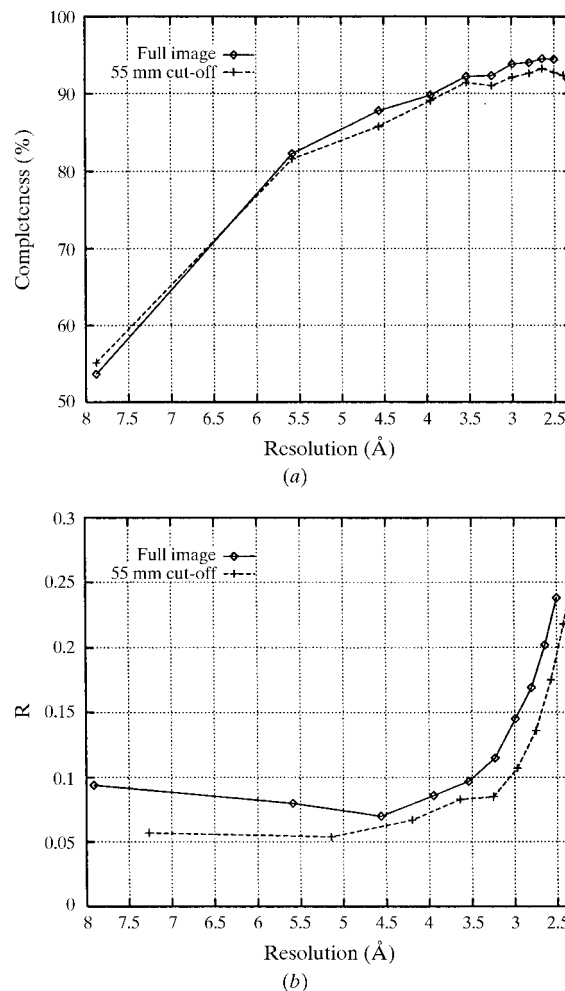

(*a*)

(*b*)

Figure 4
Comparison of (*a*) completeness and (*b*) R_{merge} when using whole area images and with 55 mm radius cut-off of images.

Table 3
X-PLOR refinement results of wild-type HMBS at 2.3 Å.

Notes: (i) The final r.m.s. deviations from ideality of bond lengths, bond angles, dihedral angles and improper angles were 0.007 Å, 1.574°, 22.934° and 1.290°, respectively. (ii) The data between 20 Å and 2.3 Å were used in refinement (except where stated otherwise). (iii) The numbers of reflections in the working set and the test set were 12533 and 1416, respectively. The number of non-H atoms in the final model being refined was 2408.

Cycle	No. of waters	*X-PLOR* refinement	R_{factor} (%)	R_{free} (%)
1	0	Rigid body (1 group, 8 Å to 4 Å)	28.6	
		Rigid body (9 groups, 8 Å to 4 Å)	27.9	
		Rigid body (9 groups, 8 Å to 2.7 Å)	29.9	
		Rigid body (9 groups, 8 Å to 2.3 Å)	31.9	
		Group temperature factors	26.4	
		Simulated annealing (3000 K, 1/2 weight†)	24.5	31.6
		Individual temperature factors	22.2	29.5
2	43	Simulated annealing (3000 K, 1/2 weight)	21.0	28.5
		Individual temperature factors	20.5	28.1
3	77	Simulated annealing (3000 K, 1/2 weight)	20.4	28.7
		Individual temperature factors	20.0	28.2
4	88	Simulated annealing (3000 K, 1/2 weight)	20.2	28.0
		Individual temperature factors	19.8	27.8
5	101	Simulated annealing (3000 K, 1/2 weight)	19.9	28.3
		Individual temperature factors	19.5	28.2
6	117	Simulated annealing (4000 K, 1/2 weight)	20.1	28.2
		Individual temperature factors	19.5	27.7
7	118	Simulated annealing (3000 K, 1/2 weight)	19.7	28.1
		Individual temperature factors	19.3	27.9
8	170	Simulated annealing (3000 K 1/2 weight)	19.0	28.7
		Individual temperature factors	18.4	28.4
9	142	XYZ refinement (1/2 weight)	19.4	26.9
		Individual temperature factors	19.1	26.9
10	145	XYZ refinement (1/2 weight)	19.2	27.0
		Individual temperature factors	18.9	26.9
Final‡	150	XYZ refinement (1/2 weight)	19.5	
		Individual temperature factors	19.4	

† Using half of the weight determined by *X-PLOR* for the X-ray pseudo energy term.   ‡ All reflections were used for the final cycle.

meters were a = 88.06, b = 75.73, c = 50.35 Å. The 'soft limits' determined from the intensity distributions of the Laue patterns (Hao, Harding & Campbell, 1995) were λ_{min} = 0.34 Å, λ_{max} = 1.6 Å and d_{min} = 2.0 Å, which were used for spot prediction. The 'spatial overlap parameter', ε, was set to 0.28 mm (half the average spot size) which would enable *INTLAUE* (see below) to deconvolute spatially overlapped reflections with centre-to-centre distances greater than ε.

INTLAUE. Diffraction spots were integrated, *i.e.* for singles, multiples and deconvoluted spatially overlapped spots. Since the spot size was consistent across the whole image, standard profiles of fixed size (6 pixels × 6 pixels) but with radial elliptical masking were used for profile fitting. Spots were rejected as saturated when even one pixel was saturated; typically for these images, 15 such saturated spots occurred per image.

LAUENORM. The wavelength-normalization curve was determined using the λ-curve method based on the fact that the same reflection or its symmetry-related ones, which should have the same final intensity (no anomalous scattering assumed), were illuminated by different wavelengths. Therefore, a curve (the 'λ-curve') could be applied to bring all the Laue data onto the same relative scale of intensity, *i.e.* independent of wavelength. At the same time, inter-image scale factors and isotropic temperature factors were calculated to put the data from different images onto

the same relative scale. After the wavelength-normalization curve had been determined from singles (Cruickshank *et al.*, 1987), the deconvolution of energy multiples was carried out (Campbell & Hao, 1993). The 47 images were divided into two subsets, *i.e.* images 1–23 (subset I) and 24–47 (subset II), and these were wavelength-normalized separately (owing to the matrix limits of the *LAUENORM* program). The results are summarized in Table 2. The wavelength-normalization curve and inter-image scale factors (for example, for subset I) are shown in Fig. 2.

AGROVATA. Finally, the singles and deconvoluted multiples of both subsets were merged and reduced to a unique data set. These data statistics are also summarized in Table 2.

Because of the polychromatic nature of the X-ray beam, the flat-field correction performed at one wavelength (0.87 Å) is not necessarily ideal for Laue data (although this wavelength does lie in the middle of the illuminating bandpass used here). Fig. 3 shows the residual effect (in terms of $I_{reference}/I_{Laue}$) of one of the 47 images after applying the non-uniformity correction. A residual effect is still visible, particularly at the corners of the CCD. Therefore, the data-processing procedures mentioned above were repeated with an image radius cut-off of 55 mm (*i.e.* spots predicted to occur beyond a radius of 55 mm were rejected). Results are also shown in Table 2. Fig. 4 shows

the completeness and R_{merge} breakdown against resolution for 'whole area' images *versus* 'radius 55 mm' images.

Table 2 and Fig. 4 show that, with the use of 55 mm radius cut-off of images, R_{merge} and $I/\sigma(I)$ greatly improve with only a slight sacrifice of data completeness and redundancy. Therefore, this was the data set used for the protein structure refinement of the wild-type HMBS (see below). Moreover, the resolution could be extended to 2.3 Å [from the 2.5 Å initially set as a reasonable resolution limit based on R_{merge} and $I/\sigma(I)$]. R_{merge} for the deconvoluted multiples was 6%, *versus* 10% for the singles, showing the effectiveness of the deconvolution procedure and of course the greater preponderence of strong reflection intensities in the deconvoluted set *versus* singles set [$\langle I/\sigma(I) \rangle$ being 8 *versus* 5, respectively]. The completeness between ∞ and $2d_{\mathrm{min}}$ increased from 66% to 78% *via* the addition of deconvoluted multiples, which also improved the completeness between $2d_{\mathrm{min}}$ and d_{min}, typically adding 90 extra unique reflection intensities per equal resolution annulus of $\sim$1100 reflections. The final data set used to 2.3 Å resolution had an overall R_{merge} of 10.2% and the data completeness was 77.5, 91.7 and 89.8% for ∞–$2d_{\mathrm{min}}$, $2d_{\mathrm{min}}$–d_{min} and ∞–d_{min}, respectively.

4. Wild-type HMBS structure refinement

The initial protein model used was the MAD-derived model of SeMet-labelled HMBS (at room temperature) having been refined at 2.4 Å with R_{factor} = 17% (Hädener *et al.*, 1999; PDB code 1AH5) but with Se atoms replaced by S atoms and without any water molecules. The *X-PLOR* program (Brunger, 1992) was used for structure refinement. An 'R-free' set with 10% of the total number of reflections ($\sim$1400 reflections) was flagged and left out of structure refinement. No σ cut-off of data was applied throughout refinement, *i.e.* no weak data were discarded. Simulated annealing refinement was used in almost every refinement cycle with the advantage of its enhanced radius of convergence. After each cycle of protein model refinement, the 'R-free' set was added back to the working set for map calculation.

The *O* program (Jones *et al.*, 1991) was used to examine electron density maps ($2F_o − F_c$ and $F_o − F_c$) and the

Table 4
The overall r.m.s. deviation of atomic positions between the wild-type HMBS Laue model and the SeMet-labelled HMBS MAD model, both in the reduced form.

Note that the very mobile regions were excluded from the calculation in order to obtain more sensitive atomic shifts about the more rigid regions. The excluded regions were residues 3, 40–42, 60–62, 240–244 and 305–313.

C_α atoms	
Domain 1	0.246 Å
Domain 2	0.341 Å
Domain 3	0.300 Å
Overall	0.289 Å
All protein atoms	
Domain 1	0.569 Å
Domain 2	0.676 Å
Domain 3	0.528 Å
Overall	0.588 Å

model manually adjusted after each cycle of *X-PLOR* refinement. The *PROCHECK* (Laskowski *et al.*, 1993) program was used to check the stereochemical quality of the model. *PEAKMAX* and *WATERPEAK* (Collaborative Computational Project, Number 4, 1994) were used to locate possible water molecules. The *X-PLOR* refinement details, cycle by cycle, are summarized in Table 3. The *PROCHECK* results for the final protein model showed that, among the 251 non-glycine and non-proline residues, 231 residues (92.0%) are located in the most favoured regions and 20 residues (8.0%) in the additional allowed regions in the Ramachandran plot. The N-terminal residues, Met1 and Leu2, that are close to the protein surface, were invisible and so is a loop region between residues 43 and 59 (TRGDVILDTPLAKVGGK). The C-terminal residues are not well defined, *i.e.* residue numbers 308 to 313; interestingly these are seen in the MAD structure of SeMet-HMBS (Hädener *et al.*, 1999) but not in the structure of the oxidized form (Louie *et al.*, 1992). The electron density for the cofactor (reduced position) is very well defined. Although there is some weak electron density around the second ring position of the oxidized cofactor (see Fig. 5), the cofactor is mainly in its reduced state.

The real-space R-factors (RSRs) (Kleywegt & Jones, 1996) are shown in Fig. 6. The RSRs of most residues are of good quality (below 30%), except for the N-terminus, the C-terminus and regions near the 42–60 loop and the 241–
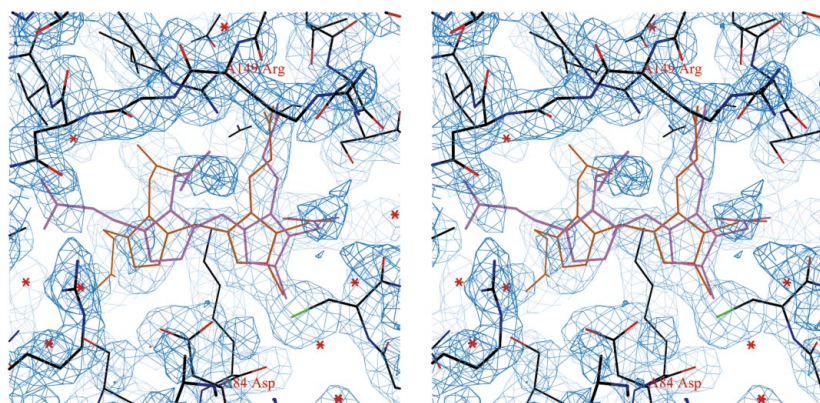

Figure 5
$2F_o − F_c$ stereo electron density map contoured at 1.0 r.m.s. around the dipyrromethane cofactor. Note that there is weak density around the second ring of the oxidized cofactor position (in magenta).

Table 5
Number of overloaded intensity spots summed over the 47 Laue images .

Column (*a*) with zero pixels allowed to be saturated per spot, and column (*b*) with 8 pixels allowed to be saturated per spot. Notes: (i) A 'typical' image of the 47 images recorded contained ~4500 spots, up to a radius of 55 mm, with an $\langle I/\sigma(I) \rangle$ of 8, with 3400 spots having $I > 3\sigma(I)$ and 100 spots with $I > 10\sigma(I)$. Overall the strongest reflection without overload had F_{calc} = 991 (the 061 reflection) and the strongest reflection of all was the 200 reflection with F_{calc} = 16129 {these F_{calc} values should be squared to yield I_{calc} so that to fully capture the dynamic range of these data a further factor of approximately 256 [*i.e.* $(16129/991)^2$] would be needed from the detector dynamic range performance, which is already 16 bits deep, *i.e.* it should ideally be 24 bits deep}. (ii) Each spot covered ~6 × 6 pixels = 36 in size. 1 pixel = 114 μm. (iii) The mean intensity of spots that were multiples was typically four times greater than spots that were singles. (iv) Estimation of spot intensities with a modest number of pixels saturated (up to 8 out of 36 shown here) was performed *via* a new profile-fitting algorithm of one of us (QH). The Laue image data used for the refinement did not include these. Nevertheless, column (*b*) shows that software alone cannot solve this problem of saturated spot intensity estimation but warrants further detector hardware development.

Laue spot type	(*a*)	(*b*)
Singles	152	83
Multiples	336	205
Singles (spatial overlaps)	79	16
Multiples (spatial overlaps)	105	44
Totals	672	348
Average number per Laue image	15	8

243 loop region. The overall r.m.s. deviations of atomic positions between the wild-type reduced form and the seleniomethionine-labelled reduced form (PDB code 1AH5; Hädener *et al.*, 1999) were also calculated but with some very mobile regions excluded in order to obtain more sensitive atomic shifts about the more rigid regions. They are shown in Table 4.

5. Discussion and concluding remarks

High-quality Laue data were collected at the ESRF ID09 with their CCD detector and processed with the Daresbury Laue software. Laue data of high completeness at low resolution (*e.g.* 77.5% between ∞ and $2d_{min}$) was successfully measured through the fine-angular-interval data-collection strategy made possible with the use of the CCD rapid readout and its high DQE and high-quality multiples deconvolution *via* the λ_{curve} method. The high quality and completeness of these data yielded a refined protein atomic model which has very good stereochemistry and RSR
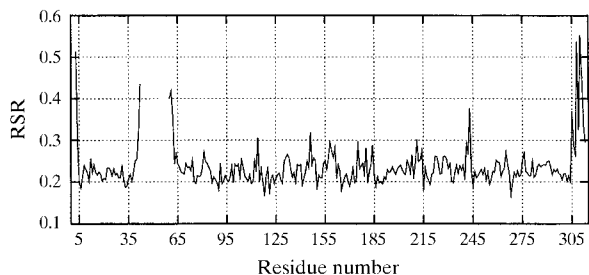

Figure 6
Real-space *R*-factor (RSR-factor) per amino acid residue.

factors as well as excellent $2F_o - F_c$ electron density maps. The non-uniformity correction of CCD images worked well but there was still a residual effect, particularly near the corners of the CCD. The 55 mm radius cut-off of the images improved the quality of the final data without sacrificing data completeness. It should be mentioned that the Daresbury Laue software is now gathered in the form of just two programs (*LAUEGEN* and *LSCALE*), and many improvements have been made since the original release in the late 1980s (see Arzt *et al.*, 1999, and references therein).

To investigate where the 10.2% of missing data resided between ∞ and d_{min}, 22.5% between ∞ and $2d_{min}$, comprising ~1400 and ~390 reflections, respectively, examination of the low-resolution sampling efficiency of the 2.5° angle-interval strategy (for 47 such spaced images) was made (see Appendix *A*). This utilized the term 'd_{all}' [introduced by Weisgerber (1993)], being the lowest resolution at which *all* RLPs (reciprocal lattice points) within the sampled region of reciprocal space come into the diffraction position, which is a function of the experimental data-collection parameters λ_{max}, λ_{min}, and the angle sampling interval. In the case studied here, d_{all} is ~11.5 Å and the theoretically sampled volume fraction between ∞ and 11.5 Å should be 79%. The actual completeness between ∞ and 11.5 Å is 28.7% (*i.e.* some 32 reflections out of 111 possible). Between ∞ and $2d_{min}$ the actual missing low-resolution data comprise 22.5%. Appendix *A*1 shows that this is not due to poor geometric sampling when a fine angle interval is used since this should only be a 0.91% loss in this case. So the 22.5% loss basically lies elsewhere. To examine where/how these losses occurred, comparison was made with the calculated structure factors. Some multiples will be of weak intensity and cause problems for the deconvolution algorithm. Weak reflections will always cause problems but have relatively less impact on the electron density map. The rejection of strong Laue spots, where merely a single saturated pixel in the program *INTLAUE* constituted grounds for rejection in each Laue image integration, is a more serious worry. For the final data set used for the model refinement the electron density map correlation coefficient is 83% (*versus* 100% for the 'perfect' calculated map). Overall then, were the missing reflections predominantly 'saturated' ones? For ∞ to d_{all} for the strongest half of those F_{calc}s, 85% were indeed missing in the final observed data set. One Laue image, under the conditions of measurement in Table 1, contained on average 15 saturated spots, *i.e.* 672 saturated spots for all 47 Laue images [Table 5, column (*a*)]. Clearly, a detector with a bigger dynamic range would be valuable. Alternatively, profile shape estimation in the software of saturated spots would recover a subset of the saturated spots [*i.e.* up to about 50% of them in these images; see Table 5, column (*b*)]. To capture saturated spots, another approach would be to have a short and a long exposure for each and every crystal orientation; whilst this might be feasible for cyclic time-resolved experiments of reversible structural processes, this is not desirable for the time-resolved

diffraction study of irreversible processes unless CCD detector readout times could be shortened. The 'pixel' detector, however, offers both bigger dynamic range and faster readout, and looks an attractive development for time-resolved protein crystallography.

APPENDIX *A*
The theoretical aspects of the fine-angular interval Laue data-collection strategy

*A*1. *The low-resolution hole*

One of the most striking features of structural studies using Laue data has been the systematic lack of completeness at low resolution. Several effects can contribute to this.

(i) The volume in reciprocal space that is sampled in any Laue exposure narrows into a cusp towards the origin, *i.e.* towards the lowest resolution. Between exposures the crystal is rotated by an angle $\Delta\varphi$ around the spindle axis. This angle will always be larger than the opening angle of the cusp which, in the limit, is effectively zero. Therefore at lowest resolutions a proportion of reciprocal lattice points (RLPs) does not come into the diffraction position at all.

(ii) Low-resolution diffraction spots are of higher average intensity than high-resolution reflections. Exposure times are usually chosen to achieve as high a resolution for the dataset as possible. Therefore a significant proportion of low-resolution reflections may be saturating the detector, especially in cases where a detector with rather a limited dynamic range is used (*i.e.* such as film). These so-called overloads are discarded in data processing.

(iii) In the case of a polychromatic beam, Bragg's law can be satisfied for a given θ not only by reflection (d, λ) but also by any reflection $(d/n, \lambda/n)$ where n is an integer. A reflection $(d/n, \lambda/n)$ will contribute to the same diffraction spot if $d/n \geq d_{\min}$ and $\lambda_{\min} \leq \lambda/n \leq \lambda_{\max}$. Such a Laue reflection is called a multiple reflection or multiplet because it consists of several (individual) Bragg reflections.
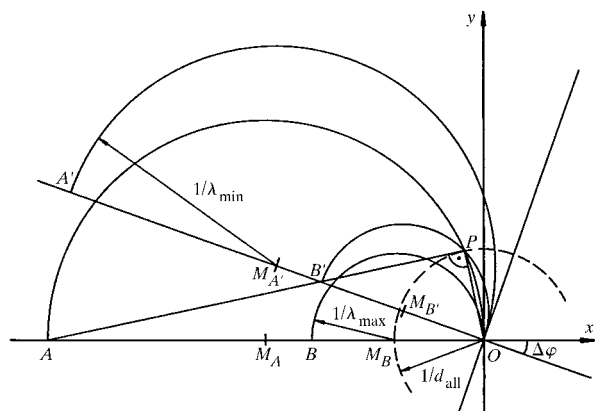
RLPs that give rise to a multiplet lie firstly on a straight line that passes through the origin of reciprocal space, and secondly within the volume that is stimulated in the particular crystal orientation.

For a long time it was assumed that the multiplicity problem affected the majority (or even all) of Laue spots (*e.g.* see Bragg, 1975). But Cruickshank *et al.* (1987) showed that, even in the most unfavourable case of an infinite bandpass, 73%, *i.e.* the majority of RLPs, are single.

There are, however, methods to retrieve the reflection intensities in multiple Laue spots. This is especially worthwhile and beneficial for the completeness of the dataset if the experiment is performed using a broad bandpass.

(i) The first method when using film as the detector, with the diffraction pattern recorded on a whole pack of films, used the wavelength-dependence of the film absorption factor whereby each component of a multiple diffraction spot is attenuated to a different extent. This formed the basis of the Daresbury Laue Suite program *UNSCRAM* which deconvoluted doubles with reasonable quality (Helliwell, Habash *et al.*, 1989).

(ii) Multiples have been deconvoluted in a direct-methods approach which is based on the Patterson function and Sayre's equation (Hao *et al.*, 1993). Multiples can also be deconvoluted in a maximum entropy approach (Xie & Hao, 1997), which does not require data redundancy and can therefore be of particular interest for time-resolved studies on a short time scale.

(iii) In this paper, in a modified version of the Daresbury Laue Suite program *LAUENORM*, deconvolution of multiples has been based on the variation of the wavelength-normalization curve (Helliwell, 1992; Campbell &
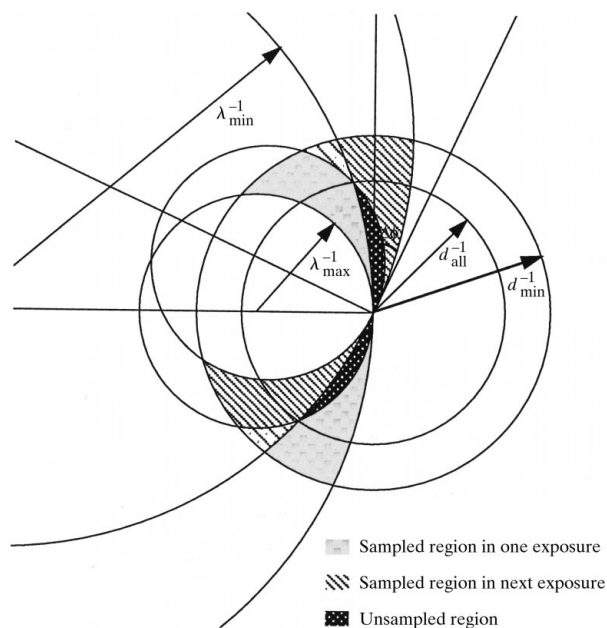
Figure 7
Ewald sphere construction for two Laue exposures at $\varphi = 0$ and $\varphi = \Delta\varphi$; the φ axis is perpendicular to the plane of the page. P denotes the points where the stimulated volumes connect, and its distance from the origin of reciprocal space is $1/d_{\text{all}}$.

Figure 8
The two-dimensional projection of the unsampled region between two adjacent exposures in Laue diffraction.

Hao, 1993). Campbell *et al.* (1994) explored the impact on protein electron density maps for the (artificial) case of zero completeness between ∞ and $2d_{min}$ and then the positive impact of deconvoluted multiples (no singles) being added between ∞ and $2d_{min}$. This method has now also been adopted in other Laue packages.

As was evident from the data-processing statistics in Table 2, the λ-curve deconvolution method of Campbell & Hao (1993) proved satisfactory. However, since in each image some 15 Laue spots saturated the detector, these probably accounted for the missing low-resolution reflections referred to in the main text. To be sure, however, of the details of the geometric sampling of reciprocal space the unsampled volume of reciprocal space (V_{hole}) is analysed in the next two sections of this Appendix.

A2. Incomplete sampling of low-resolution data ($\infty > d \geq d_{all}$) in a typical Laue experiment: derivation of an equation for d_{all}

As described in §A1, reciprocal space is not sampled evenly in the Laue method. The volume contained in the three limiting spheres narrows sharply towards the origin. The resolution up to which reciprocal space is sampled incompletely can be calculated from $\Delta\varphi$ and the wavelength range, and a derivation of the required equation is given below.

Fig. 7 illustrates the situation and introduces some parameters which are used in the derivation. P is the point where the $1/\lambda_{min}$ sphere of one exposure and the $1/\lambda_{max}$ sphere of the next exposure intersect, *i.e.* where the volumes that are stimulated in the two exposures connect. Its distance from the origin of reciprocal space is equal to $1/d_{all}$, where d_{all} is the (lowest) resolution at which *all* RLPs within the sampled section of reciprocal space come into the diffraction position.

In the following, the position of P in reciprocal space is calculated and then d_{all} as the distance of P from the origin. P lies on the intersection of (i) the $1/\lambda_{min}$ limiting sphere centred at M_A and (ii) the $1/\lambda_{max}$ limiting sphere centred at $M_{B'}$. According to Thales' law,† the points $0, P, A$ form a triangle with a right angle at P, and so do the points O, P, B'. Consequently P lies on the straight line $y = m_1x + c$ through A' and B' and also on the straight line $y = m_2x$ which passes through the origin and has a slope $m_2 = -1/m_1$.

A2.1. Calculation of m_1 and c_1.

$$A = (-2/\lambda_{min}, 0),$$

$$B' = [-2\cos(\Delta\varphi)/\lambda_{max}, 2\sin(\Delta\varphi)/\lambda_{max}],$$

$$\begin{aligned} m_1 &= (B'_y - A_y)/(B'_x - A_x) \\ &= [2\sin(\Delta\varphi)/\lambda_{max}]/[-2\cos(\Delta\varphi)/\lambda_{max} + 2/\lambda_{min}] \\ &= \sin(\Delta\varphi)/[-\cos(\Delta\varphi) + \lambda_{max}/\lambda_{min}], \end{aligned}$$

† Thale's law: given a circle, any triangle with all three vertices on the circumference of the circle such that one of the sides of the triangle is a diameter of the circle has a right angle at the vertex opposite the diameter.

$$\begin{aligned} c_1 &= A_y - m_1A_x \\ &= \{-\sin(\Delta\varphi)/[-\cos(\Delta\varphi) + \lambda_{max}/\lambda_{min}]\}(-2/\lambda_{min}) \\ &= 2\sin(\Delta\varphi)/[\lambda_{max} - \lambda_{min}\cos(\Delta\varphi)]. \end{aligned}$$

A2.2. Calculation of P_x and P_y.

P is the point where the straight lines $y = m_1x + c_1$ and $y = m_2x = -x/m_1$ intersect,

$$\begin{aligned} &\{\sin(\Delta\varphi)/[-\cos(\Delta\varphi) + \lambda_{max}/\lambda_{min}]\}P_x \\ &\quad + \{2\sin(\Delta\varphi)/[\lambda_{max} - \lambda_{min}\cos(\Delta\varphi)]\} \\ &= \{[-\cos(\Delta\varphi) + \lambda_{max}/\lambda_{min}]/-\sin(\Delta\varphi)\}P_x \\ &\Leftrightarrow P_x\{\sin(\Delta\varphi)/[-\cos(\Delta\varphi) + \lambda_{max}/\lambda_{min}] \\ &\quad + [-\cos(\Delta\varphi) + \lambda_{max}/\lambda_{min}]/\sin(\Delta\varphi)\} \\ &= -2\sin(\Delta\varphi)/[\lambda_{max} - \lambda_{min}\cos(\Delta\varphi)]. \end{aligned}$$

Now substitute

$$\begin{aligned} k &= \sin(\Delta\varphi)/[\lambda_{max}/\lambda_{min} - \cos(\Delta\varphi)] = m_1 \\ &\Rightarrow P_x(k + 1/k) = -2k/\lambda_{min} \\ &\Leftrightarrow P_x = -2k/[\lambda_{min}(k + 1/k)] = -2/[\lambda_{min}(1 + 1/k^2)] \end{aligned}$$

$$P_y = -P_x/k = -P_x/m_1 = 2/[\lambda_{min}(k + 1/k)].$$

A2.3. Calculation of d_{all}.

$$\begin{aligned} d_{all} &= (P_x^2 + P_y^2)^{-1/2} = (P_x^2 + P_x^2/k^2)^{-1/2} \\ &= 1/[|P_x|(1 + 1/k^2)^{1/2}] \\ &= [\lambda_{min}(1 + 1/k^2)]/[2(1 + 1/k^2)^{1/2}] \\ &= \lambda_{min}(1 + 1/k^2)^{1/2}/2, \end{aligned}$$

i.e.

$$d_{all} = \lambda_{min}(1 + 1/k^2)^{1/2}/2, \tag{1}$$

where

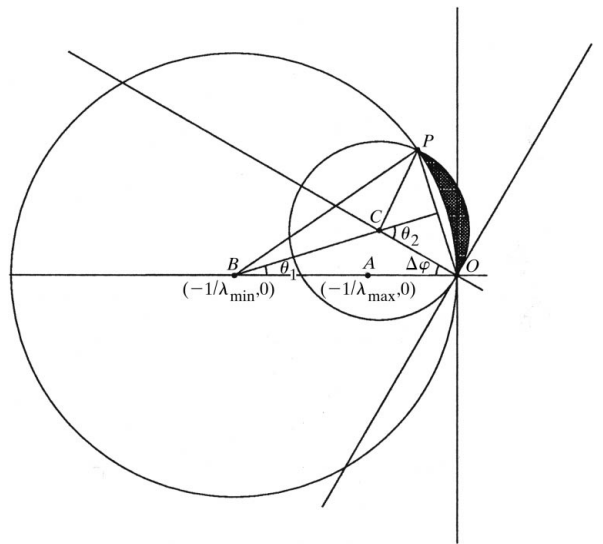**Figure 9**
Simplified demonstration of the two-dimensional projection of the unsampled region between two adjacent exposures in Laue diffraction.

Table 6
Summary of d_{all} and the volume of the unsampled region at different angular intervals with $\lambda_{max} = 1.45$ Å, $\lambda_{min} = 0.45$ Å and $d_{min} = 2.0$ Å.

$\Delta\varphi$	2.5°	5°	7°	14°	25°
d_{all}	11.47 Å	5.75 Å	4.12 Å	2.11 Å	1.25 Å
% of unsampled region:					
Relative to d_{min}	0.11%	0.62%	1.70%	12.98%	–
Relative to $2d_{min}$	0.91%	4.94%	13.59%	–	–
Relative to d_{all}	21.35%	14.67%	14.88%	15.16%	16.11%

$$k = \sin(\Delta\varphi)/[\lambda_{max}/\lambda_{min} - \cos(\Delta\varphi)].$$

A2.4. Examples. (i) Narrow bandpass: $\lambda_{min} = 0.5$ Å, $\lambda_{max} = 0.9$ Å, $\Delta\varphi = 5° \Rightarrow d_{all} = 2.32$ Å.

(ii) Broad bandpass: $\lambda_{min} = 0.3$ Å, $\lambda_{max} = 1.5$ Å, $\Delta\varphi = 10° \Rightarrow d_{all} = 3.47$ Å.

(iii) Very broad bandpass: $\lambda_{min} = 0.3$ Å, $\lambda_{max} = 2.6$ Å, $\Delta\varphi = 10° \Rightarrow d_{all} = 6.64$ Å.

A3. Derivation of the unsampled volume V_{hole} for finite $\Delta\varphi$

The unsampled region consists of two parts (*i.e.* the top and bottom parts, see a two-dimensional demonstration in Fig. 8) with equal volume. The volume (V_{hole}) of each part of the unsampled reciprocal region between two adjacent exposures is also a function of the angular interval, λ_{max} and λ_{min}, and is derived as below. For simplicity only the top half is considered. The overall volume of the unsampled region between two adjacent exposures is simply $2V_{hole}$.

The unsampled reciprocal region between two adjacent exposures shown in Fig. 8 is simply the intersecting region between the sphere of $1/\lambda_{min}$ at one exposure and the sphere of $1/\lambda_{max}$ at the next exposure (Fig. 9). The unsampled volume is the difference volume between two 'caps' which are created through cutting the two spheres by a plane passing O and P with the normal vector $\vec{BC}$. The volume of the 'cap' is

$$V_{cap} = \pi R^3 \int_0^\theta \sin^3\theta\, d\theta, \qquad (2)$$

where R is the radius of the corresponding sphere, θ is half the central angle spanned by the projection of the cap on the xy plane, and

$$\int_0^\theta \sin^3\theta\, d\theta = (-\sin^2\theta\cos\theta - 2\cos\theta + 2)/3. \qquad (3)$$

Therefore, the next step is to calculate θ values for each of the two 'caps'.

As C is the rotation of A by $\Delta\varphi$, its coordinate is $(-\cos\Delta\varphi/\lambda_{max}, \sin\Delta\varphi/\lambda_{max})$. Therefore,

$$\overline{BC} = [(-\cos\Delta\varphi/\lambda_{max} + 1/\lambda_{min})^2 + (\sin\Delta\varphi/\lambda_{max})^2]^{\frac{1}{2}}$$
$$= [(1/\lambda_{max})^2 + (1/\lambda_{min})^2 - (2\cos\Delta\varphi/\lambda_{max}\lambda_{min})]^{1/2}, \quad (4)$$

$$\cos\theta_1 = [(1/\lambda_{min})^2 + (\overline{BC})^2 - (1/\lambda_{max})^2]/2\overline{BC}(1/\lambda_{min})$$
$$= (1/\lambda_{min} - \cos\Delta\varphi/\lambda_{max})/\overline{BC},$$

$$\theta_1 = \cos^{-1}[(1/\lambda_{min} - \cos\Delta\varphi/\lambda_{max})/\overline{BC}], \qquad (5)$$

$$\theta_2 = \theta_1 + \Delta\varphi. \qquad (6)$$

So the unsampled volume (V_{hole}) is

$$\left[\pi(1/\lambda_{max})^3\int_0^{\theta_2}\sin^3\theta\, d\theta\right] - \left[\pi(1/\lambda_{min})^3\int_0^{\theta_1}\sin^3\theta\, d\theta\right].$$

Substitute equation (3) we obtain

$$V_{hole} = \pi\{(1/\lambda_{max})^3[(-\sin^2\theta_2\cos\theta_2 - 2\cos\theta_2 + 2)/3]$$
$$- (1/\lambda_{min})^3[(-\sin^2\theta_1\cos\theta_1 - 2\cos\theta_1 + 2)/3]\}. \qquad (8)$$

The percentage of the unsampled region (V_{hole}) *versus* the reciprocal space covered in the angular width $\Delta\varphi$ of the sphere of d_{min}^{-1}, *i.e.* $(4\pi/3)(1/d_{min}^3)(\Delta\varphi/2\pi)$ is simply

$$V_{hole}/[(4\pi/3)(1/d_{min}^3)(\Delta\varphi/2\pi)]. \qquad (9)$$

The percentage of the unsampled region (V_{hole}) *versus* the sphere of d_{min}^{-1} can thus be calculated (Table 6). Likewise, V_{hole} can be compared with the volume of the $2d_{min}$ sphere (*i.e.* ∞ to $2d_{min}$ is a low-resolution sphere of data) or the volume of the d_{all} sphere itself.

As Table 6 shows, by using the fine-angular interval strategy, the actual unsampled region is reduced from 13% (relative to d_{min}) at 14° to only 0.11% at 2.5° (0.91% relative to $2d_{min}$). At 2.5° $\Delta\varphi$ the sampled region of the d_{all} sphere should be 79%.

If the overall angular range covered is greater than 90°, part of the unsampled region at one angular setting will be illuminated at other angular settings at least 90° away. Therefore, the values shown in Table 6 are the worst case. The unsampled region is therefore reduced. Moreover, if internal symmetries of the crystal exist, the symmetry-related region of unsampled reciprocal space will possibly be covered. So in terms of data completeness, the situation should in practice be better than Table 6 shows.

The advantages of using a small angular interval strategy (*e.g.* 5° or less) are not only from the improvement of completeness at low resolution but also from the high redundancy of high-resolution data. This latter will benefit the determination of the wavelength-normalization curve and also the deconvolution of energy multiples. These calculations show, however, that for the HMBS Laue data described here, with $d_{all} = 11.5$ Å for a $\Delta\varphi$ of 2.5° the actual completeness between ∞ and $2d_{min}$ is worse (77.5%) than the prediction based on V_{hole} (99.1%). Between ∞ and d_{all} (11.5 Å) the actual completeness is 28.7% *versus* 78.65% expected (at worst), where the number of reflections possible would be 111, all likely to be strong reflections. Hence, the most likely 'loss of yield' stages in the data acquisition are the detector dynamic range limitation or the processing steps of the software package (*i.e.* poor treat-

ment of saturated spots, *e.g.* spots with only one pixel value saturated are rejected at the integration stage).

References

Arzt, S., Campbell, J. W., Harding, M. M., Hao, Q. & Helliwell, J. R. (1999). *J. Appl. Cryst.* **32**, 554–562.

Battersby, A. R. & Leeper, F. (1990). *Chem. Rev.* **90**, 1261–1274.

Bolduc, J. M., Dyer, D. H., Scott, W. G., Singer, P., Sweet, R. M., Koshland, D. E. Jr & Stoddard, B. L. (1995). *Science*, **268**, 1312–1318.

Bourgeois, D., Nurizzo, D., Kahn, R. & Cambillau, C. (1998). *J. Appl. Cryst.* **31**, 22–35.

Bradbrook, G., Deacon, A., Habash, J., Helliwell, J. R., Helliwell, M., Nieh, Y. P., Raftery, J., Snell, E. H., Trapani, S., Thompson, A. W., Campbell, J. W., Allinson, N. M., Moon, K., Ursby, T. & Wulff, M. (1997). *Time-Resolved Diffraction*, edited by J. R. Helliwell & P. M. Rentzepis, ch. 7. Oxford University Press.

Bragg, W. L. (1975). *The Development of X ray Analysis*, edited by D. C. Phillips & H. Lipson, p. 137. London: G. Bell & Sons.

Brunger, A. (1992). *X-PLOR.* Version 3.1. Yale University, USA.

Cameron, A. D., Smerdon, S. J., Wilkinson, A. J., Habash, J., Helliwell, J. R., Li, T. & Olson, J. S. (1993). *Biochemistry*, **32**, 13061–13070.

Campbell, J. W. (1995). *J Appl. Cryst.* **28**, 228–236.

Campbell, J. W., Deacon, A., Habash, J., Helliwell, J. R., McSweeney, S., Hao, Q., Raftery, J. & Snell, E. (1994). *Bull. Mater. Sci. Indian Acad. Sci.* **17**, 1–18.

Campbell, J. W., Habash, J., Helliwell, J. R. & Moffat, K. (1986). *Inf. Quart. Prot. Cryst.*, No. 18, pp. 23–31. Warrington: Daresbury Laboratory.

Campbell, J. W. & Hao, Q. (1993). *Acta Cryst.* **A49**, 889–893.

Campbell, J. W., Hao, Q., Harding, M. M., Nguti, N. D. & Wilkinson, C. (1998). *J. Appl. Cryst.* **31**, 496–502.

Chayen, N. E., Boggon, T. J., Cassetta, A., Deacon, A., Gleichmann, T., Habash, J., Harrop, S. J., Helliwell, J. R., Nieh, Y. P., Peterson, M. R., Raftery, J., Snell, E. H., Hädener, A., Niemann, A. C., Siddons, D. P., Stojanoff, V., Thompson, A. W., Ursby, T. & Wulff, M. (1996). *Q. Rev. Biophys.* **29**(3), 227–278.

Collaborative Computational Project, Number 4 (1994). *Acta Cryst.* **D50**, 760.

Cruickshank, D. W. J., Helliwell, J. R. & Johnson, L. N. (1992). Editors. *Time-Resolved Macromolecular Crystallography.* The Royal Society and Oxford University Press.

Cruickshank, D. W. J., Helliwell, J. R. & Moffat, K. (1987). *Acta Cryst.* **A43**, 656–674.

Edwards, C., Palmer, S. B., Emsley, P., Helliwell, J. R., Glover, I. D., Harris, G. W. & Moss, D. S. (1990). *Acta Cryst.* **A46**, 315–320.

Gomez de Anderez, D., Helliwell, M., Habash, J., Dodson, E. J., Helliwell, J. R., Bailey, P. D. & Gammon, R. E. (1989). *Acta Cryst.* **B45**, 482–488.

Hädener, A., Matzinger, P. K., Battersby, A. R., McSweeney, S., Thompson, A. W., Hammersley, A. P., Harrop, S. J., Cassetta, A., Deacon, A., Hunter, W. N., Nieh, Y. P., Raftery, J., Hunter, N. & Helliwell, J. R. (1999). *Acta Cryst.* **D55**, 631–643.

Hädener, A., Matzinger, P. K., Malashkevich, V. N., Louie, G. V., Wood, S. P., Oliver, P., Alefounder, P. R., Pitt, A. R., Abell, C. & Battersby, A. R. (1993). *Eur. J. Biochem.* **211**, 615–624.

Hao, Q., Campbell, J. W., Harding, M. M. & Helliwell, J. R. (1993). *Acta Cryst.* **A49**, 528–531.

Hao, Q., Harding, M. M. & Campbell, J. W. (1995). *J. Appl. Cryst.* **28**, 447–450.

Helliwell, J. R. (1979). Daresbury Laboratory Study Weekend, DL/Sci/R13, pp. 1–6. Warrington: Daresbury Laboratory.

Helliwell, J. R. (1991). *Nucl. Instrum. Methods*, **A308**, 260–266.

Helliwell, J. R. (1992). *Macromolecular Crystallography with Synchrotron Radiation.* Cambridge University Press.

Helliwell, J. R., Habash, J., Cruickshank, D. W. J., Harding, M. M., Greenhough, T. J., Campbell, J. W., Clifton, I. J., Elder, M., Machin, P. A., Papiz, M. Z. & Zurek, S. (1989). *J. Appl. Cryst.* **22**, 483–497.

Helliwell, J. R., Nieh, Y. P., Raftery, J., Cassetta, A., Habash, J., Carr, P. D., Ursby, T., Wulff, M., Thompson, A. W., Niemann, A. C. & Haedener, A. (1998). *J. Chem. Soc. Faraday Trans.* **94**(17), 2615–2622.

Helliwell, J. R. & Rentzepis, P. M. (1997). Editors. *Time-Resolved Diffraction.* Oxford University Press.

Helliwell, M., Gomez de Anderez, D., Habash, J., Helliwell, J. R. & Vernon, J. (1989). *Acta Cryst.* **B45**, 591–596.

Howell, P. L., Almo, S. C., Parsons, M. R., Hajdu, J. & Petsko, G. (1992). *Acta Cryst.* **B48**, 200–207.

Jones, T. A., Zou, J. Y., Cowan, S. W. & Kjeldgaard, M. (1991). *Acta Cryst.* **A47**, 110.

Kleywegt, G. J. & Jones, T. A. (1996). *Acta Cryst.* **D52**, 829–832.

Laskowski, R. A., Macarthur, M. W., Moss, D. S. & Thornton, J. M. (1993). *J. Appl. Cryst.* **26**, 283–291.

Lindahl, M., Liljas, A., Habash, J., Harrop S. & Helliwell, J. R. (1992). *Acta Cryst.* **B48**, 281–285.

Louie, G. V., Brownlee, P. D., Lambert, R., Cooper, J. B., Blundell, T. L., Wood, S. P., Warren, M. J., Woodcock, S. C. & Jordan, P. M. (1992). *Nature (London)*, **359**, 33–39.

Maginn, S. J., Harding, M. M. & Campbell, J. W. (1993). *Acta Cryst.* **B49**, 520–524.

Moy, J. P., Hammersley, A. P., Svensson, S. O., Thompson, A., Brown, K., Claustre, L., Gonzalez, A. & McSweeney, S. (1996). *J. Synchrotron Rad.* **3**, 1–5.

Peterson, M. R., Harrop, S. J., McSweeney, S. M., Leonard, G. A., Thompson, A. W., Hunter, W. N. & Helliwell, J. R. (1996). *J. Synchrotron Rad.* **3**, 24–34.

Ren, Z., Bourgeois, D., Helliwell, J. R., Moffat, K., Srajer, V. & Stoddard, B. L. (1999). *J. Synchrotron Rad.* **6**, 891–917.

Ren, Z. & Moffat, K. (1994). *J. Synchrotron Rad.* **1**, 78–82.

Ren, Z. & Moffat, K. (1995a). *J. Appl. Cryst.* **28**, 461–481.

Ren, Z. & Moffat, K. (1995b). *J. Appl. Cryst.* **28**, 482–493.

Rossmann, M. G. (1979). *J. Appl. Cryst.* **12**, 225–238.

Schlichting, I., Almo, S. C., Rapp, G., Wilson, K., Petratos, K., Lentfer, A., Wittinghofer, A., Kabsch, W., Pai, E. F., Petsko, G. A. & Goody, R. S. (1990). *Nature (London)*, **345**, 309–315.

Shrive, A. K., Clifton, I. J., Hajdu, J. & Greenhough, T. J. (1990). *J. Appl. Cryst.* **23**, 169–174.

Singer, P. T., Smalas, A., Carty, R. P., Mangel, W. F. & Sweet, R. M. (1993). *Science*, **259**, 669–673.

Srajer, V., Teng, T.-Y., Ursby, T., Pradervand, C., Ren, Z., Adachi, S., Schildkamp, W., Bourgeois, D., Wulff, M. & Moffat, K. (1996). *Science*, **274**, 1726–1729.

Weisgerber, S. (1993). PhD thesis, The University of Manchester, UK.

Xie, Y. & Hao, Q. (1997). *Acta Cryst.* A**53**, 643–648.

Yang, X. J., Ren, Z. & Moffat, K. (1998). *Acta Cryst.* D**54**, 367–377.